Lattice Dynamics and Thermodynamic Properties of $Y_3Al_5O_{12}$ (YAG)

Markos Poulos[a], Stefanos Giaremis[a], Joseph Kioseoglou[a], John Arvanitidis[a], Dimitris Christofilos[b], Sotirios Ves[a], Markus P. Hehlen[c], Neil L. Allan[d], Chris E. Mohn[e], and Konstantinos Papagelis[a,f,*]

[a] Physics Department, Aristotle University of Thessaloniki, 54124 Thessaloniki, Greece
[b] School of Chemical Engineering & Physics Laboratory, Faculty of Engineering, Aristotle University of Thessaloniki, Thessaloniki, 54124 Greece
[c] Space & Remote Sensing (ISR-2), Mailstop B244, Los Alamos National Laboratory, Los Alamos, NM 87545, USA
[d] School of Chemistry, University of Bristol, Cantock's Close, Bristol, BS8 1TS, United Kingdom
[e] Centre for Earth Evolution and Dynamics, University of Oslo, N-0315 Oslo, Norway
[f] Institute of Chemical Engineering Sciences, Foundation of Research and Technology-Hellas (FORTH/ICE-HT), Patras 26504, Greece

[*] Corresponding Author
E-mail: kpapag@physics.auth.gr

Abstract

We present Inelastic Neutron Scattering measurements of $Y_3Al_5O_{12}$. The measured neutron-weighted phonon density-of-states and optical phonon frequencies are compared with the results from atomistic calculations within the Quasi-Harmonic Approximation (QHA) over a wide temperature range, using both first principles density functional theory calculations and also an extended empirical interatomic- potential Shell model scheme. The phonon-related thermodynamic and elastic properties calculated within the QHA are in excellent agreement with the available experimental data.

Keywords: Garnet, YAG, Lattice dynamics, Inelastic Neutron Scattering, DFT, Shell Model, Raman, Infrared, Quasi-harmonic Approximation, vibrational thermodynamics, elastic constants

1.Introduction

Yttrium-Aluminum Garnet (YAG) belongs to the rare-earth aluminum garnet family with chemical formula $RE_3A_5O_{12}$, where RE represents a trivalent rare-earth or transition metal cation (Y^{3+}, Nd^{3+}, Gd^{3+}, etc.) and A is a trivalent atom (Al^{3+}, Ga^{3+}, Fe^{3+} etc.). The general formula for the garnet family is $X_3Y_2(ZO_4)_3$ (X = Ca, Fe etc., Y = Al, Cr, etc., Z = Si, As, V, Fe, Al), where the X cations occupy lattice sites with dodecahedrally coordinated O^{2-} anions as first neighbours, the Y cations occupy octahedral sites, and the Z cations are tetrahedrally coordinated to oxygen in ZO_4 tetrahedra. For YAG, Y=Z=Al^{3+} and X=Y^{3+}. Garnets is a family of synthetic insulators with widespread uses in a variety of applications. The excellent spectroscopic, mechanical, and thermal properties of YAG render it ideal as a host crystal for near-infrared solid-state lasers. In particular Nd^{3+}-doped YAG is the most widely known such laser with applications in the commercial, medical, industrial and even the military sector [1, 2]. The combination of the host crystal's low thermal expansion, high optical transparency, low acoustic loss and high threshold for optical damage, along with high chemical and mechanical stability, high thermal conductivity [3] and hardness make it the most widely used solid-state laser material [4].

The various technological applications of rare-earth garnets are of course not restricted to host materials for solid state lasers. Temperature or pressure induced shifts in the luminescence of the Nd^{3+} dopant atoms have also been exploited for high temperature and/or pressure sensor instead of ruby [5], while RE^{3+}-doped nano-garnets have been extensively used as nano-lasers, phosphors and alternatives to quantum dots in photonic and optoelectronic devices [6]. Ferrimagnetic rare-earth garnets, mainly Yttrium Iron Garnet (YIG), have found important applications in microwave technology, mainly in optical isolators, anti-reciprocal devices [7], as well as in data storage applications [8] and in magnetic bubble memory devices [9]. Recently, lithium-stuffed garnets have found an important application as solid-state electrolytes in all-solid-state lithium batteries [10]; $Li_7La_3Zr_2O_{12}$ (LLZO)

is a superionic conductor with high electrochemical stability, two highly desirable features of ideal ionic electrolytes, making this class of materials a very promising alternative to toxic electrolytes in Li^+ batteries for renewable energy applications.

Detailed atomistic studies of the host material can provide invaluable insights into thermal, mechanical, electronic and optical properties relevant to the continuously growing number of its technological applications. Previous theoretical studies have focused mainly on the material's electronic band structure [11] as well as on the electronic properties of dopant elements in Y^{3+} sites [12, 13]. Phonon properties have been investigated either through single Γ-point calculations of the phonon spectrum at ambient conditions within the rigid-ion model [14], or through treatment of phonon pressure response within either ab-initio [15] or atomistic forcefield schemes [16]. The effect of the thermal expansion has, to the best of our knowledge, not yet been explicitly taken into consideration in the literature.

In this work, we present a detailed atomistic and experimental study of the vibrational and thermodynamic properties of YAG. Inelastic Neutron Scattering (INS) measurements at T=16 K were carried out for the first time, along with Raman and IR spectroscopic measurements of YAG at ambient conditions. A lattice dynamics theoretical treatment was performed using both ab initio (density functional theory, DFT) and Shell model empirical potential approaches. Furthermore, we have investigated the vibrational, thermodynamic, and elastic properties of YAG by employing, for the first time, the Quasi-Harmonic Approximation (QHA) for phonon calculations over a wide temperature range, from 0 to 1900 K, which is close to the material's melting point (~1940 K). We have calculated a considerable number of thermodynamic and elastic properties, IR and Raman active phonon modes, as well as one-phonon total and projected densities of states, which are then compared to our experimental findings, as well as to existing data in the literature.

2. Computational Methods

2.1 Quasi-Harmonic Approximation

In the usual Harmonic Approximation (HA), mean atomic positions $\bar{\boldsymbol{R}}_i$, force constants, and normal mode eigenfrequencies $\omega_{\mathbf{q},j}$ are fixed and calculated for the system's minimum static energy configuration, that is, at T=0, ignoring the zero-point vibrations. To account for thermal dependence arising from anharmonicity, within the framework of the Quasi-Harmonic Approximation (QHA), terms higher than second order in the potential energy expansion are still ignored, but anharmonicity and thermal expansion effects are included in the model by calculating the force constants and mode eigenfrequencies at a structural configuration which is different from the absolute equilibrium configuration. Instead, the expansion of the crystal potential Φ is made with respect to a new configuration, henceforth denoted by a set of collective structural parameters X

At any specified temperature and pressure, the optimised structure is found by direct minimisation of the (quasi-harmonic) Gibbs energy $G_{qh}(X,p,T)$. Since all calculations in the present study are for a system under ambient pressure, we set p = 0 and hence the Gibbs free energy G is equal to the Helmholtz energy $A_{qh}(X,T)$. For the equilibrium configuration, we thus require $\frac{\partial A_{qh}(X,T)}{\partial \mathrm{X}} = 0$, which gives the desired thermal dependence of the structural parameters, $X(T)$. Here, A_{qh} is the sum of static and vibrational terms and is given by

$$A_{qh}(X,T) = U_{static}(X) + \sum_{\mathbf{q},j} \frac{\hbar\omega_{\mathbf{q},j}(X)}{2} + k_B T \sum_{\mathbf{q},j} \ln\left(1 - e^{-\hbar\omega_{\mathbf{q},j}(X)/kT}\right) \quad (1)$$

The first term in the right-hand side is the potential energy of the static lattice, which is derived from appropriate empirical potentials within the Shell model scheme or is equal to the sum of the electronic internal energy $U_{el}(X)$ (the electronic ground state energy) and the static ionic Coulomb energy in the *ab initio* calculations. The second term is the zero-point energy, which includes the sum of the harmonic vibrational contributions from all the normal modes $(\mathbf{q},j)$. For weak anharmonicity, the quasi-harmonic free energy $A_{qh}(T)$ is a very good approximation to the total free energy, since it is exact to at least order $O(\Phi_4)$ in the expansion of the crystal with respect to the atomic displacements [17].

Any free structural parameter not inherently constrained by symmetry can be a member of the set of the configuration parameters X, such as the mean basis atomic positions $\bar{\boldsymbol{R}}_i$, the lattice parameter a, etc. In YAG, all cations occupy high symmetry positions and therefore the only free structural parameters to be minimized are the oxygen core and shell positions and the lattice parameter a. After minimization of A_{qh} with respect to X at each temperature, we obtain a relation $X(T)$ and consequently, all other thermodynamic quantities that can be calculated from the free energy become functions of T only.

Such quantities include, for example, the volumetric thermal expansion coefficient α_V, which can be directly calculated from the temperature dependence of $X(T)$, the vibrational heat capacities $C_V(T)$ and $C_P(T)$, and he elastic constant tensor C_{ij}, which is the second derivative of the internal energy density with respect to strain. The 21 independent elements of C_{ij} are considerably reduced by symmetry, since for a cubic material such as YAG, the only unique independent elements are C_{11}, C_{12} and C_{44} [18]. The

(isothermal) bulk modulus, $K_T = 1/\chi_T$, where $\chi_T = -\frac{1}{V}\left(\frac{\partial V}{\partial P}\right)_T$ is the isothermal compressibility and can also be calculated either directly by the second derivative of the free energy with respect to the volume, or from the elastic constant tensor C_{ij} [18]. The Shell model scheme calculates K_T via the elastic constants, while within the DFT scheme, the Helmholtz free energy $A_{qh}(V,T)$ data are fitted to the Vinet equation of state [19], to obtain the equilibrium volume $V_0(T)$ as well as the bulk modulus K_T. Finally, the average thermal Grüneisen parameter γ_{th}, which appears in the Grüneisen-Mie equation of state [20], can also be calculated from the other thermodynamic quantities stated below and it serves as a single-parameter average measure of anharmonicity, since it is related to a weighted average of the derivatives of the phonon eigenfrequencies with respect to the volume [21]. For more details on the details and the formulas used for the calculation of the thermodynamic quantities obtained in this work, see the Supporting Information (SI Section 1)

2.2 Shell Model Computational Methods

The atomistic forcefield calculations were performed with the General Utility Lattice Program (GULP) [22], using the Shell model, first introduced by Dick and Overhauser [23], in which the rigid ion core and its spherical electronic shell are coupled by a simple harmonic spring-like potential:

$$U_i^{shell} = \frac{1}{2}k_0\left(r_i^{core} - r_i^{shell}\right)^2 \quad (2)$$

where r_i^{core} and r_i^{shell} are the instantaneous positions of the core and shell of the ith atom, and k_0 is an adjustable parameter, the spring constant. In our model, only the O^{2-} ions possess shells, as they are the most polarizable.

The short-range many-body interactions between atoms are modelled by explicit empirical potentials. The two-body contribution is approximated by a Buckingham potential, given by

$$U_{ij}^{Buckingham} = Ae^{-\left(\frac{r_{ij}}{\rho_i+\rho_j}\right)} - \frac{C^{(6)}}{r_{ij}^6} \quad (3)$$

Here, ρ_i, ρ_j, and $C^{(6)}$ are adjustable parameters. Short-range potentials act between cation cores and oxygen shells, as well as between oxygen shells, but not between cation cores.

An angular contribution is also included in the form of a three-body bond-bending potential. The motivation for this is that YAG does not follow the Cauchy relations $C_{12} = C_{14}$, which a purely two-body potential model predicts, and the Al-O bonds in YAG are known to be partially covalent [11]. For simplicity, we have chosen a simple harmonic form that accounts for deviations from the expected coordination angles

$$U_{ijk}^{three} = \frac{1}{2}k_1\left(\theta_{ijk} - \theta_0\right)^2 \quad (4)$$

where θ_{ijk} is the angle between the *i*-*j*-*k* atoms, k_1 is an adjustable parameter, and $\theta_0 = 90°, 109.5°,$ and $70°$ for octahedral, tetrahedral, and dodecahedral coordination, respectively. Finally, the long-range electrostatic interaction is given by the Coulomb potential

$$U_{ij}^{Coulomb} = \frac{e^2 z_i z_j}{4\pi\varepsilon_0 r_{ij}} \quad (5)$$

where z_i are the effective charges, which are also adjustable parameters, again fulfilling the cell charge neutrality condition. The Buckingham potential parameters are similar to those reported by Milanese et al. [24] and all parameters are presented in Table 1.

In the static energy calculations, the short-range potential summations were performed by imposing a spherical cut-off radius $r_{cutoff} = 3.5$ Å, in order to include interactions up to the fourth neighbours. The electrostatic contribution, which is a slowly converging series, was calculated by the Ewald summation method [25]. The vibrational contributions to thermodynamic quantities were calculated over a 40×40×40 Monkhorst-Pack sampling grid inside the first Brillouin zone [26]. Free energy minimization was performed using a Newton-Raphson minimization algorithm [27-29] with a gradient convergence threshold of $<10^{-3}$ eV/atom, while the Hessian was updated according to the Broyden-Fletcher-Goldfarth-Shanno (BFGS) formula [30].

Table 1. Shell model potential parameters used in this work.

Buckingham	$\rho_i+\rho_j$ (Å)	A (eV)	$C^{(6)}$ (eV/Å^6)	**Coulomb**	z_i (+e)
Al_{oct}-O_{shell}	0.3118	1114.9	0.000	Al_{oct}	+ 2.9
Al_{tet}-O_{shell}	0.3205	1200.0	10.654	Al_{tet}	+ 2.9
Y-O_{shell}	0.3491	1345.1	10.000	Y	+ 3.0
O_{shell}-O_{shell}	0.149	22764.0	27.880	O_{core}	+ 0.91
				O_{shell}	- 2.86

Three-Body	k_1 (eV/deg^2)	**Shell**	k_0 (eV/Å^2)
O_{shell}-Al_{oct}-O_{shell}	2.093	O_{shell}	60
O_{shell}-Al_{tet}-O_{shell}	4.093		
O_{shell}-Y-O_{shell}	2.093		

Finally, Raman and IR active modes were determined by standard group theoretical methods. The procedure involved the construction of symmetry vectors for the point group of the wavevector $G_{\vec{k}}$. These symmetry vectors were in turn used to diagonalize the dynamical matrix into blocks belonging to a particular irreducible representation of $G_{\vec{k}}$ [31, 32], thus allowing for the symmetry assignment of the extracted mode eigenfrequencies. This was particularly useful for determining the LO-TO splitting at the Γ-point.

2.3 Ab Initio Computational Details

Ab initio calculations were performed within the framework of DFT as implemented in the Vienna *ab initio* simulation package (VASP) [33-36] by using the plane-wave basis projector augmented wave (PAW) method [37] within the revised Perdew-Burke-Ernzerhof Generalized Gradient Approximation for solids (PBEsol GGA) approach [38] on the 80 atoms comprising the primitive unit cell of the YAG structure. The plane wave energy cut off was set to 520 eV and a Gaussian smearing with a width of 0.01 eV was used for the determination of the partial occupancies in the total energy calculations. The core radii used for the PAW pseudopotentials for Y, Al, and O were 2.8 Å, 1.9 Å, and 1.52 Å, respectively, with the 4s, 4p, 5s, and 4d electrons for Y, 3s and 3p electrons for Al, and 2s and 2p electrons for O being treated as valence. The Brillouin zone of the unit cell for the electrons was sampled by Γ-centered a 4×4×4 uniform Monkhorst-Pack, Γ-centred *k*-point mesh. Convergence with respect to the *k*-point sampling and energy cut off were explicitly checked. Lattice parameters and ionic positions were relaxed with a conjugate gradient algorithm until the energy difference between two consecutive ionic steps was smaller than 10^{-10} eV and the forces in each ion were lower than 10^{-8} eV/Å.

A quasi-Newton (variable metric) algorithm is used to relax the ions into their instantaneous ground state configuration. The forces and the stress tensor are used to determine the search directions for finding the equilibrium positions. The implemented algorithm [39] implicitly calculates an approximation of the inverse Hessian matrix by considering information from previous iterations. Phonon calculations were performed with the finite displacements method as implemented in the PHONOPY package [40], with the amplitude of the inequivalent finite displacements set at 0.01 Å. After applying symmetry operations for the structure, the number of the inequivalent finite displacements for the phonon calculations was found to be 11. Phonon frequencies and thermodynamic properties were calculated within a 40×40×40, Γ-centred q-point mesh. Phonon and thermodynamic properties were calculated under the harmonic approximation, while calculations were also performed within the quasi-harmonic approximation for addressing the effect of thermal expansion. The QHA calculations were performed for hydrostatically strained structures with the lattice parameters ranging from 0.97 to 1.03 of the optimised lattice parameter. IR and Raman frequencies were calculated by using the central differences scheme based approach implemented in the Phonopy-Spectroscopy package [41]. These calculations are computationally intensive as they also require the evaluation of the dielectric tensor for positive and negative displacements along each mode, which resulted in a total of 474 different structures containing the inequivalent displacements for the 80 atoms in the primitive unit cell. The dielectric tensor of each system was evaluated by the VASP code.

3. Experimental Details

3.1 Inelastic Neutron Scattering measurements

Inelastic neutron scattering (INS) measurements were performed on the Pharos time-of-flight (TOF) spectrometer at the Manuel Lujan Jr. Neutron Scattering Center (Los Alamos National Laboratory). The sample consisted of 46 g of powder that was obtained by grinding a YAG single crystal (CASTECH Inc., Fuzhou, China). The powder was packed in a 5 mm thick aluminum can, oriented at 45° to the incident neutron beam, and cooled to 16 K with a closed-cycle Helium refrigerator. The use of such thin sample greatly reduced multi-phonon scattering, and we estimate multi-phonon scattering contributions to be <1% in the PDOS obtained from the measurements. INS spectra were measured with an incident neutron beam energy of 130 meV and an elastic energy resolution of ±0.5 meV. The TOF data were reduced to energy (E) and scattering vector (Q) histograms, and corrections for detector efficiencies, empty can scattering, and instrumental background were performed. The normalized phonon density of states (PDOS) was obtained by integrating over Q from 0 to 15 $Å^{-1}$.

The neutron-weighted projected and total DOS (NW-PDOS) $g_k^{NW}(\omega)$ and $g_{total}^{NW}(\omega)$, respectively, are related to the normal densities $g_k(\omega)$ and $g_{total}(\omega)$ through the relations [42, 43]:

$$g_k^{NW}(\omega) = \frac{d_k g_k(\omega)}{\sum_k d_k} \tag{6}$$

and

$$g_{total}^{NW}(\omega) = \sum_k g_k^{NW}(\omega) = \frac{\sum_k d_k g_k(\omega)}{\sum_k d_k} \tag{7}$$

Here k indicates the atom species: Y, Al_{oct}, Al_{tet}, and O. Al_{oct} and Al_{tet} have different projected DOS. Also, the weighted scattering power d_k is given by

$$d_k = c_k \left(\frac{\sigma_k}{m_k}\right) \tag{8}$$

where σ_k is the total neutron scattering cross-section for atomic species k, m_k its mass, and c_k its concentration ($\sum_k c_k = 1$). For Y, Al, and O, the total neutron scattering cross sections are $\sigma_Y = 7.7$ barns, $\sigma_{Al} = 1.53$ barns, and $\sigma_O = 4.232$ barns, respectively. Furthermore, in order to take into account the dependence of the spectrometer's resolution on scattering energy, the NW-PDOS has also been convoluted with a Gaussian function having an energy-dependent width $\gamma(\omega)$. The energy dependence of the spectrometer's resolution is given by

$$\gamma(\omega) = 1.52\times10^{-3}(1048.5 - \omega)^{3/2} \quad (9)$$

where both γ and ω are measured in cm^{-1}.

3.2 IR reflectance measurements

Fourier Transform Infrared (FTIR) measurements were carried out at room temperature with a Bruker vacuum spectrometer, IFS113v. All spectra from unoriented, unpolished single-crystal samples were collected in reflectance mode within the spectral range 100-5000 cm^{-1} (mid-IR and far-IR regions). The resolution was 2 cm^{-1}, and for each spectrum 64 scans were recorded. Optical constants were obtained through a Kramers-Kronig transformation of the reflectance spectrum, and the TO and LO phonon frequencies were derived from the peak positions of $\varepsilon_2(\omega)$ and $Im(-1/\varepsilon(\omega))$, respectively. Here, ε is the dielectric function, while ε_1 and ε_2 are its real and imaginary parts, respectively.

3.3 Raman measurements

Raman spectra were recorded in the back-scattering geometry using a DILOR XY-500 triple monochromator equipped with a liquid nitrogen cooled CCD detector system and an OLYMPUS microscope coupled to the entrance of the monochromator. The spectral width of the system was 2 cm^{-1}, while the 514.5 nm line of an Ar^+ laser was used for excitation, with a laser power of 1 mW on sample. The frequency scale was calibrated using a Ne calibration lamp. The Raman active phonon frequencies were obtained by fitting the spectrum with Lorentzian peak functions. In both IR and Raman studies, the $Y_3Al_5O_{12}$ single crystal used was grown by the Czochralski technique.

4. Results and Discussion

4.1 Crystal Structure

YAG has a complex crystal structure, crystallizing in the body-centred cubic (BCC) system under the $Ia\bar{3}d$ space group (No. 230). The primitive unit cell contains 4 formula units and 80 atoms in total, while the crystallographic cell is twice the size with 8 formula units. The crystallographic cell is shown in Fig. 1, in which the intricate network of coordination polyhedra is also displayed. It is immediately evident that the garnet structure is very compact, a feature which will be used later to rationalise some of its vibrational properties. In the crystallographic cell containing 160 atoms, all atoms except the O^{2-} anions occupy special Wyckoff positions, and so their local point group is an invariant subgroup of the space group of the crystal. There are 16 octahedrally coordinated Al^{3+} cations (site symmetry C_{3i}), 24 tetrahedrally coordinated Al^{3+} cations (site symmetry S_4), and 24 dodecahedrally coordinated Y^{3+} cations (site symmetry D_2); and 96 O^{2-} anions occupying general positions (no symmetry).

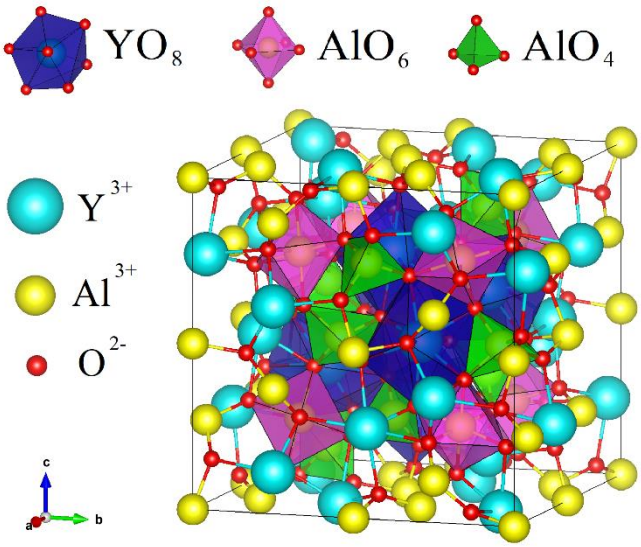

Figure 1. Crystallographic lattice cell of YAG showing the coordination polyhedra of the cations.

The fractional coordinates of these special positions are inherently fixed by symmetry, while the 96 general O^{2-} positions are determined by a set of free parameters (*x*,*y*,*z*), which can be determined experimentally. The polyhedra are not regular: the tetrahedra are stretched along one of their principal C_{3i} axes while the octahedra are stretched along the {111} cube diagonals [44]. The distortion of the dodecahedra is more complicated. Typical bond lengths at ambient conditions are 1.93 Å for the Al_{oct}-O bond and 1.82 Å for the Al_{tet}-O bond since Al atoms with different coordination numbers have different local environments with different Al-O bond lengths. The Y-O bond length varies from 2.38 to 2.46 Å due to the distortion of the dodecahedra.

4.2 Inelastic Neutron Scattering and one-phonon Density of States

The measured inelastic neutron scattering (INS) spectrum at *T*=16 K along with our theoretical calculations of neutron-weighted one-phonon densities-of-states are presented in Fig. 2. The full S(Q,E) plot is also presented in the Supplementary Information (Fig. SI-1). The theoretical phonon projected phonon densities-of-states (PDOS) are calculated at 0 K (Fig. 3) and are appropriately transformed in order to account for different neutron scattering lengths among the chemical elements Y, Al, and O comprising the crystal, as well as for the spectrometer's energy-dependent resolution. The total DOS curves in Figs. 2 and 3 normalized to unit integrated area.

As is readily evident from the graph, the agreement between both the theoretical calculations (DFT and Shell model) and the experiment is excellent, despite the complexity of the crystal structure and the experimental uncertainties

arising from the very low scattering cross sections in neutron scattering experiments. Normal modes of vibration exist in a range from 0 up to 850 cm^{-1}, while a characteristic phonon gap, found in most rare-earth garnets, is present approximately between 620 and 660 cm^{-1}, in agreement with other theoretical lattice dynamical studies [14, 15], and the recorded IR and Raman spectra presented below (Figs. 4 and 5).

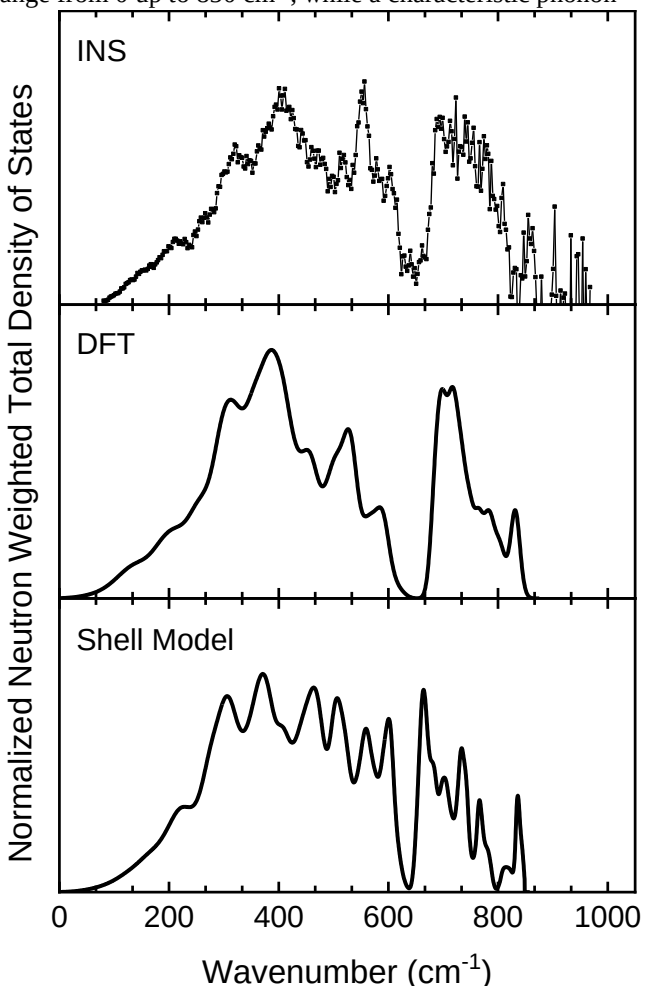

Figure 2. Experimental Inelestic Neutron Scattering (INS) at T=16 K and neutron-weighted phonon densities of states of YAG, calculated by means of DFT and the Shell model. All curves are normalized to unit area.

The signal observed in the neutron DOS spectrum above 850 cm^{-1} is instrumental noise due to increased sensitivity to background subtraction at large energy transfers, and it is within the expected magnitude.

In Fig. 3, we present the total and projected PDOS calculated from DFT and classical potentials. It should be noted that the Al_{oct} and Al_{tet} PDOS curves are magnified (x5) for better visibility, as their contributions are very small. The agreement between the two theoretical methods is very good, as they both reproduce the experimental profile with very good accuracy. In particular, the DFT method appears to better describe the energy gap and the neutron data at low energies (below the gap), while at higher energies (above the gap) both methods are in good agreement with INS results.

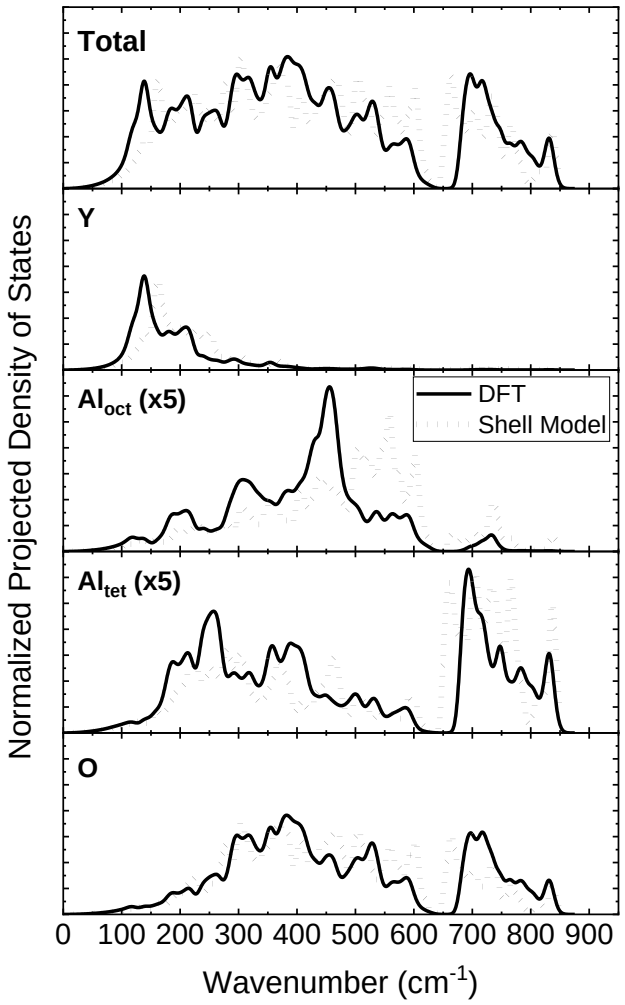

Figure 3. Calculated total and projected phonon density-of-states within DFT and the Shell model. The total DOS is normalized to unit integrated area, whereas the Al_{oct} and Al_{tet} PDOS curves have been rescaled (x5) for clarity.

Moreover, from Fig. 3 it is evident that the Shell model, compared with DFT, systematically shifts the PDOS peaks towards higher (lower) energies in the low (high) energy region of the spectrum, implying a similar behaviour in the dispersion branches, leading to a noticeable decrease in the low-high energy split in the Shell-model DOS spectrum (see Figs. SI-2 and SI-3).

By also inspecting the calculated dispersion curves (Figs. SI-2 and SI-3), we find that all modes below the prominent peak at 100-150 cm^{-1}, which is due to the lowest optical branches, belong to the three acoustic branches. As can be seen from Fig. 3, each atom species contributes differently at each spectral region. Even Al atoms with different coordination have different contributions to the total DOS. This is due to the different local environments and their symmetries. Indeed, in section 4.1 we have seen that the Al_{oct}-

O and Al_{tet}-O bond lengths vary and consequently the force constants differ. Therefore, different projected eigenvectors must be attributed to these two Al species. Fig. 3 also clearly shows that the contribution of the Al atoms is spread along the entire frequency range. Also, Y atoms contribute only over a very narrow range, between 100-250 cm^{-1} which accounts for the total DOS peak at around 100-150 cm^{-1}. By inspecting the dispersion curves, we can assign this Y vibrational contribution peak to the low-lying flat optical branches, where Y atoms have eigenvectors with significantly larger magnitude. However, this is not reflected in the Neutron Weighted DOS (Fig. 2), mainly because the Y atoms are heavy and their concentration is much smaller than that of the O atoms. Thus, from equations (7) and (8) it is evident that the weighted scattering power factor, d_Y, will be smaller for Y. In fact, $d_k = 0.0130, 0.0056, 0.0084$, and 0.1587 for Y, Al_{tet}, Al_{oct}, and O atoms, respectively, so it is clear that the neutron scattering spectrum mainly arises from the oxygen atoms (Fig. 3). Besides, the integrated area of each PDOS curve is equal to the species' relative concentration, which for O is exactly 60%.

4.3 IR and Raman active modes

Since the primitive cell of YAG contains 80 atoms, there are a total of 240 phonon modes at the Γ-point of the Brillouin zone (BZ), that can be assigned to the irreducible representations of the O_h point group as follows:

$$\Gamma = 18T_{1u} + \left(3A_{1g} + 8E_g + 14T_{2g}\right) + \left[5A_{2g} + 5A_{1u} + 5A_{2u} + 10E_u + 14T_{1g} + 16T_{2u}\right] \quad (10)$$

The $18T_{1u}$ modes are IR active (one T_{1u} corresponds to the zero-frequency acoustic mode), while the 25 modes having symmetries $3A_{1g}$, $8E_g$, and $14T_{2g}$ are Raman active. The remaining modes in square brackets are silent.

The measured Raman spectrum of YAG is shown in Fig. 4. The spectrum can be conveniently divided into three frequency regions: the low-frequency region (< 500 cm^{-1}), the intermediate region (500-600 cm^{-1}), and the high-frequency region (660-900 cm^{-1}). This is a common characteristic of the $RE_3Al_5O_{12}$ compounds [14, 45]. Site group analysis and symmetry arguments [46] reveal that A_{1g} symmetry modes exhibit molecular character and can be classified as internal and external motions of the tetrahedral AlO_4 subunits. Following this analysis [14, 46], the low-frequency modes correspond mainly to a translational motion of the heavy Y atoms with small contributions from rotational and translational motion, as well as v_3 vibrational modes, of the AlO_4 tetrahedra. The mid-frequency range modes result from the quadrupolar (v_2) molecular mode, while the high energy modes contain mainly breathing (v_1) and v_4 molecular modes of AlO_4 [47]. However, the picture from our analysis based on the extracted Raman active eigenvectors is that particularly in the mid (500-600 cm^{-1}) and low (< 500 cm^{-1}) frequency regions the oxygen motions are coupled to the cation motions. Then, the classification of the modes in terms of internal and external molecular vibrations is not applicable and such description is rather misleading.

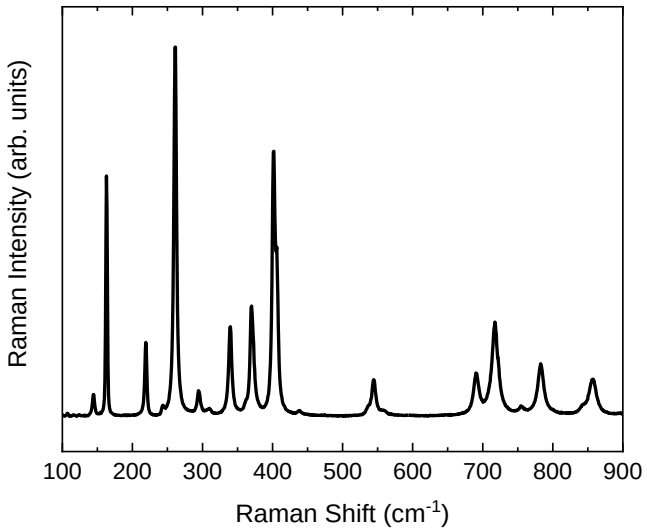

Figure 4. Raman spectrum of $Y_3Al_5O_{12}$ measured at ambient conditions.

In Table 2 we present the experimental frequencies of the Raman active modes, along with those calculated using both the Shell model and DFT. As already mentioned above, the Raman activities of these modes were determined by symmetry arguments (empirical calculations) and also through the direct calculation of the Raman tensor (DFT). The mode symmetry assignment of the experimental peaks was mainly based on the frequency values, by comparison with our theoretical calculations, and with previous studies based on high pressure [48] and polarized Raman measurements [49]. The agreement between calculated and experimentally measured values is very good.

Experimentally, we have found 24 peaks out of 25 expected. The A_{1g} and T_{2g} peaks at around 370-372 cm^{-1} are accidentally degenerate at ambient conditions but are clearly resolved at higher pressures due to their different pressure coefficients [48]. It is important to stress that two T_{2g} modes were absent in previous experimental Raman studies [48, 49]. In this work, both DFT and Shell model calculations predict (Table 2) the existence of a T_{2g} mode at around 360-365 cm^{-1}, which corresponds to the barely resolved shoulder peak at 361 cm^{-1} in the Raman spectrum of YAG (Fig. 4 and Table 2), in good agreement with previous rigid ion model calculations (~340 cm^{-1}) [48]. We predict that the last missing T_{2g} mode should lie in the range of 575-595 cm^{-1}, also in broad agreement with reference [48] (610 cm^{-1}). Its absence in the Raman spectrum of $Y_3Al_5O_{12}$ is attributed to low scattering efficiency.

Table 2. Experimentally measured and theoretically calculated Raman active mode frequencies

Mode Symmetry	ω_{calc} (cm^{-1})		ω_{exp} (cm^{-1})
	(Shell model)	*(DFT)*	
A_{1g}	363	357	370
A_{1g}	528	540	559
A_{1g}	703	766	783
E_g	176	156	163
E_g	298	306	310
E_g	360	328	340
E_g	401	386	402
E_g	512	504	523
E_g	556	513	536
E_g	659	699	712
E_g	738	754	754
T_{2g}	153	138	145
T_{2g}	224	209	220
T_{2g}	244	233	243
T_{2g}	273	251	261
T_{2g}	310	299	295
T_{2g}	364	359	361
T_{2g}	376	396	372
T_{2g}	467	424	406
T_{2g}	471	453	438
T_{2g}	549	524	545
T_{2g}	594	576	--
T_{2g}	672	691	691
T_{2g}	699	718	718
T_{2g}	834	844	857

The measured IR reflectivity spectrum is presented in Fig. 5(a), while the optical constants obtained through a Kramers-Kronig transformation, such as the real and imaginary part of the dielectric functions ε_1 and ε_2, the absorption coefficient α, and the refractive indices n and k are shown in Figs. 5(b), (c), and (d), respectively. Again, IR activity was determined both by symmetry arguments (Shell model) and also by direct calculation of the Born effective charge tensor (DFT). For the LO modes, eigenfrequencies were calculated by including the non-analytic correction terms along the {100} and {111} directions of the BZ, where $T_{1u} \rightarrow E + A_1$.

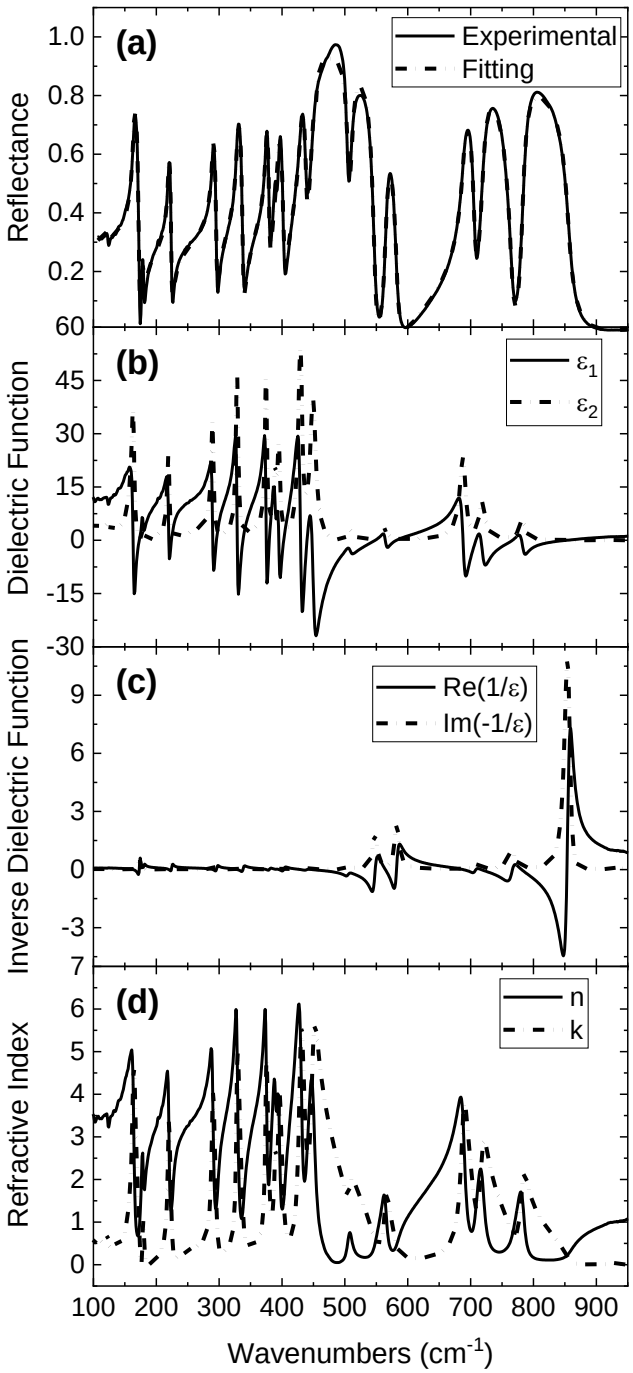

Figure 5. Infrared normal reflectivity measurements and optical constants derived by means of Kramers-Kronig transformations for $Y_3Al_5O_{12}$. (a) Measured and fitted reflectance spectrum; (b) real (ε_1) and imaginary (ε_2) part of the dielectric function, (c) $Re(1/\varepsilon)$ and $Im(-1/\varepsilon)$, where $1/\varepsilon$ is the inverse dielectric function; (d) real (n) and imaginary (k) part of the refractive index.

In Table 3 we present the LO and TO phonon frequencies calculated by both DFT and Shell model, as well as the corresponding experimentally obtained values. As it can be

Table 3. LO and TO phonon mode frequencies as calculated by both DFT and Shell model, as well as the corresponding experimentally obtained values.

ω_{TO} (cm^{-1})			ω_{LO} (cm^{-1})		
(Shell)	*(DFT)*	*(exp.)*	*(Shell)*	*(DFT)*	*(exp.)*
137	117	122	137	117	123
181	156	162	184	168	173
190	169	179	194	170	180
232	211	219	244	220	224
292	282	289	295	288	296
327	317	328	344	333	338
362	358	374	367	365	380
402	372	388	403	375	391
440	378	395	446	390	403
466	426	429	472	441	438
502	444	449	502	456	471
514	458	465	556	497	505
558	503	508	586	545	547
602	549	564	608	566	582
673	691	688	703	708	707
705	720	718	738	764	765
768	781	782	848	838	854

seen, the discrepancy between calculations and experiment is more pronounced in the frequency region 400-560 cm^{-1}, mostly for the Shell model calculations. Apart from this region, our results from DFT and empirical potentials are in very good agreement both with our experimental measurements as well as with previous experimental [50] and theoretical studies [14].

Furthermore, as observed in earlier works, the LO-TO splitting is larger for higher frequency modes; the splitting of the highest-lying mode at around 780 cm^{-1} is of the order of 70 cm^{-1}. This is also reflected in our calculations presented here.

4.4 Thermodynamic Properties

The thermodynamic properties of the YAG insulator are exclusively determined by phonon contributions. We have calculated by employing the Quasi-Harmonic Approximation the lattice parameter a, the volumetric thermal expansion coefficient α_V, the entropy S, the heat capacity at constant pressure C_p, the isothermal bulk modulus K_T, and the thermal Grüneisen parameter γ_{th}, and compared them with experimentally obtained values. All calculations were performed at constant pressure ($p = 0$). Furthermore, using the Shell model and based on the QHA, we were also able to calculate the temperature dependence of the three independent elastic constants C_{11}, C_{12}, and C_{44} over a wide temperature range. There is excellent agreement between the results and the available experimental data in the literature (see Supporting Information, SI).

The temperature dependence of the lattice parameter a, obtained through the QHA free energy minimization procedure, is plotted in Fig. 6 and compared with data from X-ray powder diffraction measurements [51]. The agreement is evidently excellent, especially for the ab initio calculations. Not only is the deviation in the lattice parameter always less than 0.2%, but the DFT calculated temperature dependence of the expansion coefficient is almost identical to the experimental one found in the literature (Fig. 7), as discussed below.

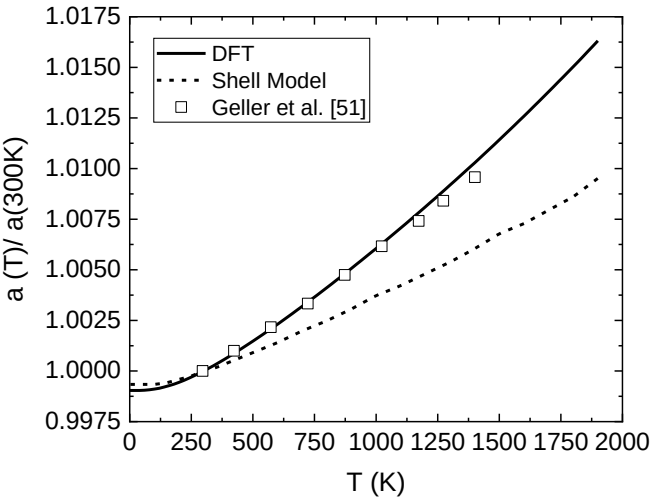

Figure 6. Calculated relative lattice parameter a(T)/a(300K) of $Y_3Al_5O_{12}$ as a function of temperature, along with the experimental X-ray powder diffraction data by Geller et al. [51].

The calculated thermal expansion coefficient α_V as a function of temperature is depicted in Fig. 7 and is compared to high-precision interferometric measurements in the temperature range 80-300 K [52] and 300-600 K [53], respectively. Note that in these references, the linear expansion coefficient α_L was measured. This is related to the volume coefficient by the simple relationship

$$\alpha_V = 3\alpha_L. \quad (11)$$

The agreement is again excellent, particularly for the ab initio calculations, where theoretical predictions practically overlap with experiment. Evidently, α_V increases monotonically over the entire range, with a large, almost constant slope at temperatures up to approximately 300 K and a considerably smaller slope for higher temperatures up to the melting temperature of ~1940 K. It is also evident that the Shell model systematically underestimates the thermal expansion

coefficient over the entire temperature range considered, but the qualitative trend is the same.

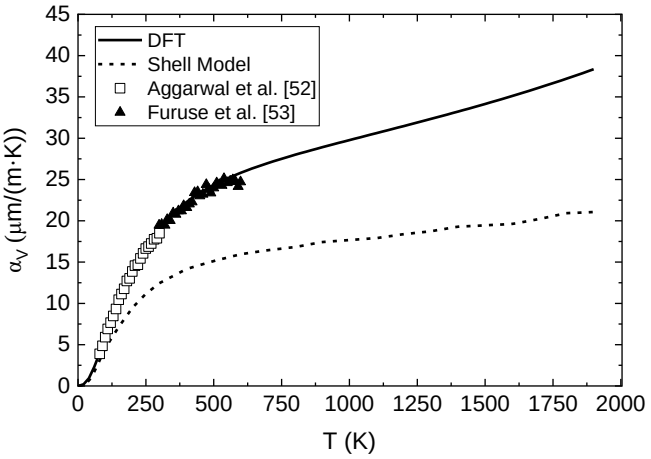

Figure 7. Calculated thermal expansion coefficient α_V of $Y_3Al_5O_{12}$ along with that obtained experimentally from interferometric measurements as a function of temperature [52, 53].

The temperature dependence of the molar heat capacity per formula unit, C_p, of YAG was also calculated and illustrated in Fig. 8 in comparison with low [54] and high [55] temperature experimental data. Here, ab-initio and Shell model calculations are in excellent agreement with each other, as well as with the experimental values, especially at lower temperatures. It is worth noting that the agreement with experiment is amazingly good even at very high temperatures close to the melting point, suggesting the Quasi-Harmonic Approximation still holds at these temperatures, which in turn implies that anharmonic effects in YAG remain weak up to the melting point. This is likely to be related with the compact, dense crystal structure, and the absence of large bond lengths at which the quasi-harmonic approximation breaks down, as observed previously in calculations using the QHA at high pressure where the bond lengths are shorter [56, 57]. From the experimental values of C_p, it is also possible to calculate the molar entropy by integration and compare it to the theoretical values calculated by the QHA. The agreement is again remarkable (Fig. SI-4).

The isothermal bulk modulus K_T, a measure of the material's elastic properties and readily obtainable from lattice dynamics calculations of the free energy, has been also calculated, and it is compared to high precision Brillouin scattering measurements of elastic constants of YAG [58] in Fig. 9. The agreement is again very good, particularly for the results obtained by DFT, which deviate from experiment at room temperature by only 0.13%. In contrast, the shortcoming of the Shell model is apparent, as it systematically overestimates the temperature dependence of K_T.

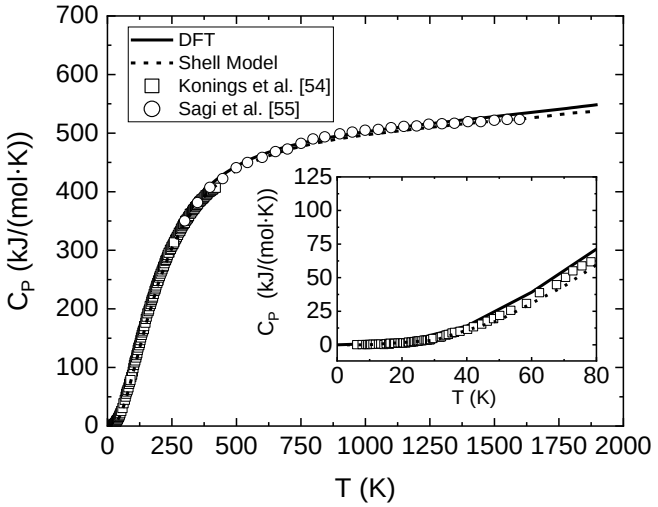

Figure 8. Molar heat capacity C_p per formula unit of YAG, as calculated within the QHA, and compared with experiment at low [54] and high [55] temperatures. The behavior of C_p below 80 K is shown magnified in the inset.

In Table 4 we present the results of the calculations by means of both DFT and the Shell model for the elastic constants C_{11}, (C_{11}-C_{12})/2, and C_{44} at 300 K, in comparison with direct Brillouin scattering measurements by Stoddart et al. [58]. The agreement is quite satisfactory, with the DFT results being again closer to experiment at room temperature (Table 4). The Shell model calculations systematically overestimate both the bulk modulus and the elastic constants, which can be attributed to the sensitivity of the short-range components of the empirical potential to variations in interatomic distances induced by strain since the elastic constants are mainly affected by short-range interactions. Additionally, in Fig. SI-5 the variation of the three independent elastic constants

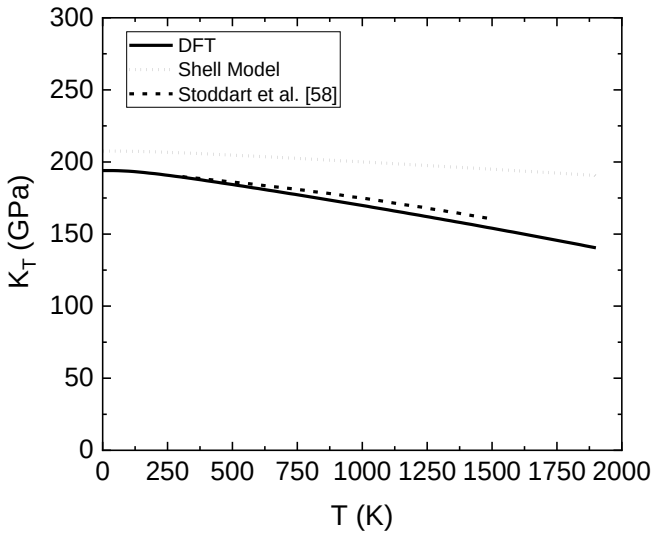

Figure 9. Calculated values of the isothermal bulk modulus K_T of $Y_3Al_5O_{12}$ *vs* T and experimental data by Stoddart et al. [58]

C_{11}, C_{12}, and C_{44} with temperature, obtained only using the Shell model, is also compared with experimental data [58].

Table 4. Calculated elastic constants at 300 K compared with those obtained from the Brillouin scattering measurements of Stoddart et al [58].

Elastic Constants (GPa)	**DFT**	**Shell model**	**Stoddart et al [58]**
C_{11}	319	365	339
$(C_{11} - C_{12})/2$	109	119	111
C_{44}	107	137	116

Finally, the temperature dependence of the thermal Grüneisen parameter γ_{th} was also calculated and is presented in Fig. 10. At 300 K, DFT calculations give a value $\gamma_{th} = 1.33$ and the Shell model gives $\gamma_{th} = 1.96$, while the experimental value obtained by thermal data is reported to be 1.43 [59]. These findings clearly demonstrate the low anharmonicity of YAG and thus further support the validity of QHA for YAG at high temperatures even close to the melting point.

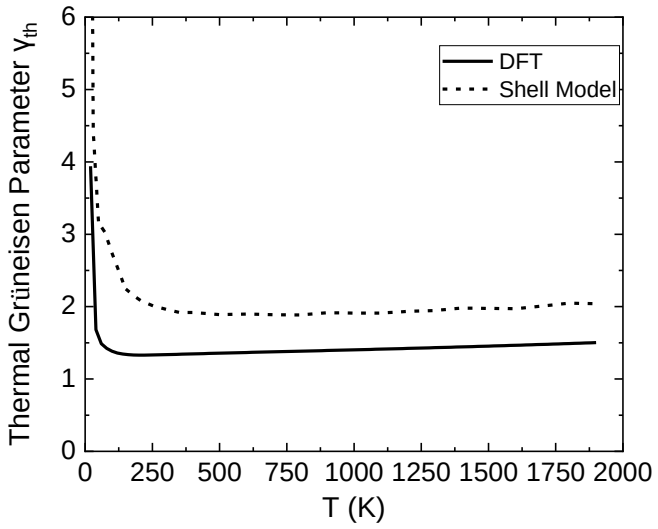

Figure 10: Calculated thermal Grüneisen parameter γ_{th}.

5. Conclusions

We have conducted a detailed experimental and theoretical lattice dynamical study of YAG and its phonon-related thermodynamic properties. The phonon spectrum has been experimentally probed by IR and Raman scattering measurements and for the first time by Inelastic Neutron Scattering. The results are overall in excellent agreement with atomistic DFT and classical potential calculations. The accuracy of both atomistic methods has additionally allowed us to calculate a range of thermodynamic and elastic properties of YAG, including the thermal expansion by employing the Quasi-Harmonic Approximation. Our atomistic calculations shows a very good description of the aforementioned properties when compared with experimental results from the litterature, even at temperatures close to the melting point. The validity of the Quasi-Harmonic Approximation, combined with the low Grüneisen coefficient of YAG implies weak anharmonicity for this system. We attributed this behaviour to the compact and dense garnet crystal structure (e.g. mineral garnets are commonly found in metamorphic rocks, i.e., they are formed at high pressures) as well as the relatively smaller bond lengths in YAG.

Acknowledgements

We would like to thank Ms T. Zorba for her technical assistance in the IR measurements. This work benefited from the use of the Pharos beamline at the Lujan Center at Los Alamos Neutron Science Center, funded by the Department of Energy (DOE) Office of Basic Energy Sciences and by Los Alamos National Laboratory (LANL) funded by the DOE under Contract No. W-7405-ENG-36. We thank Dr. F.R. Trouw (LANL) for assistance with the inelastic neutron scattering experiments. C.E.M. is funded by the Research Council of Norway's Centers of Excellence Project (223272)

References

[1] R.C. Powell, Physics of solid-state laser materials, AIP Press/Springer, New York, 1998.
[2] W. Koechner, Solid-State Laser Engineering, Springer-Verlag, New York, 2006.
[3] P.A. Giesting, A.M. Hofmeister, Thermal conductivity of disordered garnets from infrared spectroscopy, Phys. Rev. B, 65 (2002) 144305.
[4] B. Henderson, R.H. Bartram, Crystal-Field Engineering of Solid-State Laser Materials, Cambridge University Press, Cambridge, 2009.
[5] U.R. Rodríguez-Mendoza, S.F. León-Luis, J.E. Muñoz-Santiuste, D. Jaque, V. Lavín, Nd3+-doped Ca3Ga2Ge3O12garnet: A new optical pressure sensor, J. Appl. Phys., 113 (2013) 213517.
[6] V. Venkatramu, M. Giarola, G. Mariotto, S. Enzo, S. Polizzi, C.K. Jayasankar, F. Piccinelli, M. Bettinelli, A. Speghini, Nanocrystalline lanthanide-doped Lu3Ga5O12garnets: interesting materials for light-emitting devices, Nanotechnology, 21 (2010) 175703.
[7] J.F. Dillon, Magnetic and optical properties of rare earth garnets, J. Magn. Magn. Mater., 84 (1990) 213-221.
[8] W. Prandl, T. Brückel, The Spin Glass State in Garnet Mixed Crystals: New Evidence from Neutron Scattering and Macroscopic Measurements, in: Structural and Magnetic Phase Transitions in Minerals, Springer New York, New York, 1988, pp. 208-216.
[9] A.H. Bobeck, Properties and Device Applications of Magnetic Domains in Orthoferrites, Bell Syst. tech., 46 (1967) 1901-1925.
[10] S. Ramakumar, C. Deviannapoorani, L. Dhivya, L.S. Shankar, R. Murugan, Lithium garnets: Synthesis, structure,

Li + conductivity, Li + dynamics and applications, Prog. Mater. Sci., 88 (2017) 325-411.
[11] Y.-N. Xu, W.Y. Ching, Electronic structure of yttrium aluminum garnet(Y3Al5O12), Phys. Rev. B, 59 (1999) 10530-10535.
[12] S. Sugano, Y. Tanabe, H. Kamimura, Multiplets of transition-metal ions in crystals, Academic Press, New York, 1970.
[13] A. Lupei, V. Lupei, S. Grecu, C. Tiseanu, G. Boulon, Crystal-field levels of Tm3+in gadolinium gallium garnet, J. Appl. Phys., 75 (1994) 4652-4657.
[14] K. Papagelis, G. Kanellis, S. Ves, G.A. Kourouklis, Lattice Dynamical Properties of the Rare Earth Aluminum Garnets (RE3Al5O12), Phys. Status Solidi B, 233 (2002) 134-150.
[15] V. Monteseguro, P. Rodríguez-Hernández, R. Vilaplana, F.J. Manjón, V. Venkatramu, D. Errandonea, V. Lavín, A. Muñoz, Lattice Dynamics Study of Nanocrystalline Yttrium Gallium Garnet at High Pressure, J. Phys. Chem. C, 118 (2014) 13177-13185.
[16] P. Goel, R. Mittal, N. Choudhury, S.L. Chaplot, Lattice dynamics and Born instability in yttrium aluminum garnet, Y3A15O12, J. Phys. Condens. Matter, 22 (2010) 065401.
[17] G. Leibfried, W. Ludwig, Theory of Anharmonic Effects in Crystals, in: F. Seitz, D. Turnbull (Eds.) Solid State Phys., Academic Press, Boston, 1961, pp. 275-444.
[18] J.F. Nye, Physical Properties of Crystals: Their Representation by Tensors and Matrices, Clarendon Press, Oxford, 1957.
[19] P. Vinet, J.H. Rose, J. Ferrante, J.R. Smith, Universal features of the equation of state of solids, J. Phys. Condens. Matter, 1 (1989) 1941-1963.
[20] M. Born, K. Huang, Dynamical Theory of Crystal Lattices, Clarendon Press, Oxford, 1988.
[21] T.H.K. Barron, Grüneisen parameters for the equation of state of solids, Ann. Phys., 1 (1957) 77-90.
[22] J.D. Gale, GULP: A computer program for the symmetry-adapted simulation of solids, J. Chem. Soc. Faraday Trans., 93 (1997) 629-637.
[23] B.G. Dick, A.W. Overhauser, Theory of the Dielectric Constants of Alkali Halide Crystals, Phys. Rev., 112 (1958) 90-103.
[24] C. Milanese, V. Buscaglia, F. Maglia, U. Anselmi-Tamburini, Disorder and Nonstoichiometry in Synthetic Garnets A3B5O12(A = Y, Lu−La, B = Al, Fe, Ga). A Simulation Study, Chem. Mater., 16 (2004) 1232-1239.
[25] P.P. Ewald, Die Berechnung optischer und elektrostatischer Gitterpotentiale, Ann. Phys., 369 (1921) 253-287.
[26] H.J. Monkhorst, J.D. Pack, Special points for Brillouin-zone integrations, Phys. Rev. B, 13 (1976) 5188-5192.
[27] J.D. Gale, Analytical Free Energy Minimization of Silica Polymorphs, J. Phys. Chem. B, 102 (1998) 5423-5431.
[28] M.B. Taylor, G.D. Barrera, N.L. Allan, T.H.K. Barron, Free-energy derivatives and structure optimization within quasiharmonic lattice dynamics, Phys. Rev. B, 56 (1997) 14380-14390.
[29] M.B. Taylor, G.D. Barrera, N.L. Allan, T.H.K. Barron, W.C. Mackrodt, SHELL - a code for lattice dynamics and structure optimisation of ionic crystals, Comput. Phys. Commun., 109 (1998) 135-143.
[30] D.F. Shanno, Conditioning of Quasi-Newton Methods for Function Minimization, Math. Comput., 24 (1970) 647-656.
[31] A.A. Maradudin, S.H. Vosko, Symmetry Properties of the Normal Vibrations of a Crystal, Rev. Mod. Phys., 40 (1968) 1-37.
[32] G.Y. Lyubarskii, The Application of Group Theory in Physics, Pergamon, Oxford, 1960.
[33] G. Kresse, J. Hafner, Ab initio molecular dynamics for liquid metals, Phys. Rev. B, 47 (1993) 558-561.
[34] G. Kresse, J. Furthmüller, Efficient iterative schemes for ab-initio total energy calculations using a plane-wave basis set, Phys. Rev. B, 54 (1996) 11169-11186.
[35] G. Kresse, J. Furthmüller, Efficiency of ab-initio total energy calculations for metals and semiconductors using a plane-wave basis set, Comput. Mater. Sci., 6 (1996) 15-50.
[36] G. Kresse, J. Hafner, Ab initio molecular-dynamics simulation of the liquid-metal–amorphous-semiconductor transition in germanium, Phys. Rev. B, 49 (1994) 14251-14269.
[37] P.E. Blöchl, Projector augmented-wave method, Phys. Rev. B, 50 (1994) 17953-17979.
[38] J.P. Perdew, A. Ruzsinszky, G.I. Csonka, O.A. Vydrov, G.E. Scuseria, L.A. Constantin, X. Zhou, K. Burke, Restoring the density-gradient expansion for exchange in solids and surfaces, Phys. Rev. Lett., 100 (2008) 136406.
[39] P. Pulay, Convergence acceleration of iterative sequences. the case of scf iteration, Chem. Phys. Lett., 73 (1980) 393-398.
[40] A. Togo, I. Tanaka, First principles phonon calculations in materials science, Scr. Mater., 108 (2015) 1-5.
[41] J.M. Skelton, L.A. Burton, A.J. Jackson, F. Oba, S.C. Parker, A. Walsh, Lattice dynamics of the tin sulphides SnS2, SnS and Sn2S3: vibrational spectra and thermal transport, Phys. Chem. Chem. Phys., 19 (2017) 12452-12465.
[42] K. Papagelis, J. Arvanitidis, K. Prassides, S. Margadonna, Inelastic neutron scattering study of the intermolecular vibrational modes of Ba4C60, Chem. Phys. Lett., 377 (2003) 125-130.
[43] P. Brüesch, Phonons: Theory and Experiments II, Springer-Verlag, Berlin/Heidelberg, 1986.
[44] Landolt-Börnstein, Numerical Data and Functional Relationships in Science and Technology Group III, Springer-Verlag, Berlin/Heidelberg, 1978.
[45] K. Papagelis, S. Ves, Vibrational properties of the rare earth aluminum garnets, J. Appl. Phys., 94 (2003) 6491-6498.
[46] K. Papagelis, G. Kanellis, J. Arvanitidis, G.A. Kourouklis, S. Ves, Phonons in Rare-Earth Aluminum Garnets and Their Relation to Lattice Vibration of AlO4, Phys. Status Solidi B, 215 (1999) 193-198.
[47] G. Herzberg, J.W.T. Spinks, K.P. Huber, Molecular Spectra and Molecular Structure: Infrared and Raman spectra of polyatomic molecules, Prentice-Hall, New York, 1939.

[48] J. Arvanitidis, K. Papagelis, D. Christofilos, H. Kimura, G.A. Kourouklis, S. Ves, High pressure Raman study of Y3Al5O12, Phys. Status Solidi B, 241 (2004) 3149-3154.
[49] J.P. Hurrell, S.P.S. Porto, I.F. Chang, S.S. Mitra, R.P. Bauman, Optical Phonons of Yttrium Aluminum Garnet, Phys. Rev., 173 (1968) 851-856.
[50] A.M. Hofmeister, K.R. Campbell, Infrared spectroscopy of yttrium aluminum, yttrium gallium, and yttrium iron garnets, J. Appl. Phys., 72 (1992) 638-646.
[51] S. Geller, G.P. Espinosa, P.B. Crandall, Thermal expansion of yttrium and gadolinium iron, gallium and aluminum garnets, J. Appl. Crystallogr., 2 (1969) 86-88.
[52] R.L. Aggarwal, D.J. Ripin, J.R. Ochoa, T.Y. Fan, Measurement of thermo-optic properties of Y3Al5O12, Lu3Al5O12, YAIO3, LiYF4, LiLuF4, BaY2F8, KGd(WO4)2, and KY(WO4)2 laser crystals in the 80–300K temperature range, J. Appl. Phys., 98 (2005) 103514.
[53] H. Furuse, R. Yasuhara, K. Hiraga, Thermo-optic properties of ceramic YAG at high temperatures, Opt. Mater. Express, 4 (2014) 1794.
[54] R.J.M. Konings, R.R. van der Laan, A.C.G. van Genderen, J.C. van Miltenburg, The heat capacity of Y3Al5O12 from 0 to 900K, Thermochim. Acta, 313 (1998) 201-206.
[55] S. Sagi, S. Hayun, High-temperature heat capacity of SPS-processed Y3Al5O12 (YAG) and Nd:YAG, J. Chem. Thermodyn., 93 (2016) 123-126.
[56] G.D. Barrera, M.B. Taylor, N.L. Allan, T.H.K. Barron, L.N. Kantorovich, W.C. Mackrodt, Ionic solids at elevated temperatures and high pressures: MgF2, J. Chem. Phys., 107 (1997) 4337-4344.
[57] I.T. Todorov, N.L. Allan, M.Y. Lavrentiev, C.L. Freeman, C.E. Mohn, J.A. Purton, Simulation of mineral solid solutions at zero and high pressure using lattice statics, lattice dynamics and Monte Carlo methods, J. Phys. Condens. Matter, 16 (2004) S2751-S2770.
[58] P.R. Stoddart, P.E. Ngoepe, P.M. Mjwara, J.D. Comins, G.A. Saunders, High-temperature elastic constants of yttrium aluminum garnet, J. Appl. Phys., 73 (1993) 7298-7301.
[59] Y.K. Yogurtcu, A.J. Miller, G.A. Saunders, Elastic behaviour of YAG under pressure, J. Phys. C: Solid State Phys., 13 (1980) 6585-6597.